

Publications

---

8-14-2009

## Propagation of Tsunami-Driven Gravity Waves into the Thermosphere and Ionosphere

Michael P. Hickey

*Embry-Riddle Aeronautical University, hicke0b5@erau.edu*

G. Schubert

*Institute of Geophysics and Planetary Physics, University of California*

R. L. Walterscheid

*The Aerospace Corporation*

Follow this and additional works at: <https://commons.erau.edu/publication>



Part of the [Atmospheric Sciences Commons](#)

---

### Scholarly Commons Citation

Hickey, M. P., G. Schubert, and R. L. Walterscheid (2009), Propagation of tsunami-driven gravity waves into the thermosphere and ionosphere, *J. Geophys. Res.*, 114, A08304, doi: <https://doi.org/10.1029/2009JA014105>

This Article is brought to you for free and open access by Scholarly Commons. It has been accepted for inclusion in Publications by an authorized administrator of Scholarly Commons. For more information, please contact [commons@erau.edu](mailto:commons@erau.edu).

# Propagation of tsunami-driven gravity waves into the thermosphere and ionosphere

M. P. Hickey,<sup>1</sup> G. Schubert,<sup>2</sup> and R. L. Walterscheid<sup>3</sup>

Received 27 January 2009; revised 14 May 2009; accepted 8 June 2009; published 14 August 2009.

[1] Recent observations have revealed large F-region electron density perturbations ( $\sim 100\%$ ) and total electron content (TEC) perturbations ( $\sim 30\%$ ) that appear to be correlated with tsunamis. The characteristic speed and horizontal wavelength of the disturbances are  $\sim 200$  m/s and  $\sim 400$  km. We describe numerical simulations using our spectral full-wave model (SFWM) of the upward propagation of a spectrum of gravity waves forced by a tsunami, and the interaction of these waves with the F-region ionosphere. The SFWM describes the propagation of linear, steady-state acoustic-gravity waves in a nonisothermal atmosphere with the inclusion of eddy and molecular diffusion of heat and momentum, ion drag, Coriolis force, and height-dependent mean winds. The tsunami is modeled as a deformation of our model lower boundary traveling at the shallow water wave speed of 200 m/s with a maximum vertical displacement of 50 cm and described by a modified Airy function in the horizontal direction. The derived vertical velocity spectrum at the surface describes the forcing at the lower boundary of the SFWM. A steady-state 1-D ionospheric perturbation model is used to calculate the electron density and TEC perturbations. The molecular diffusion strongly damps the waves in the topside ( $>300$ -km altitude) ionosphere. In spite of this, the F-region response is large, with vertical displacements of  $\sim 2$  to 5 km and electron density perturbations of  $\sim 100\%$ . Mean winds have a profound effect on the ability of the waves to propagate into the F-region ionosphere.

**Citation:** Hickey, M. P., G. Schubert, and R. L. Walterscheid (2009), Propagation of tsunami-driven gravity waves into the thermosphere and ionosphere, *J. Geophys. Res.*, 114, A08304, doi:10.1029/2009JA014105.

## 1. Introduction

[2] *Hines* [1972] first suggested that a tsunami could generate atmospheric gravity waves that propagate up into the ionosphere and thereby produce an ionospheric perturbation that could serve as a signature for early tsunami detection. Subsequent modeling by *Peltier and Hines* [1976] supported the plausibility of this suggestion. The feasibility that a tsunami could generate atmospheric gravity waves is because of the fact that the tsunami characteristic speed ( $\sim 200$  m/s, the shallow water wave speed), wavelength (100s of km) and period (10s of minutes) lies within the range of medium-scale atmospheric gravity waves, allowing a coupling between the two motions. Additionally, a tsunami is coherent over extremely long distances with wave fronts typically a few thousand km in length. This line source would thus produce waves that propagate upward with only modest geometric spreading, thus increasing their

expected amplitudes at high altitudes and increasing their probability of detection.

[3] Using measurements of TEC from the GPS network in Japan, *Artru et al.* [2005a] reported observations of an ionospheric disturbance following a tsunami generated by the  $M = 8.2$  Peru earthquake of 23 June 2001. The tsunami and the ionospheric disturbance had similar characteristics in terms of arrival time, wave front orientation, and horizontal velocity. Numerical modeling of the event reproduced features seen in the observations, with a modeled phase speed of 221 m/s versus the observed phase speed of 150 m/s. Because the gravity waves were undamped, unrealistically large vertical displacements ( $\sim 200$  km at 400 km altitude) were obtained.

[4] *Artru et al.* [2005b] performed a study of ionospheric perturbations following the 23 June 2001 tsunami generated by a strong earthquake in Peru. Analysis of total electron content measurements obtained from the GEONET GPS network in Japan revealed perturbations having a dominant period of 20 to 30 min and having other characteristics (such as phase speed) similar to that of the tsunami. The maximum amplitude of the TEC perturbations was about 1% of the undisturbed mean, while the amplitude of the tsunami in the open ocean was 1 to 2 cm.

[5] *Lee et al.* [2008] correlated ionospheric measurements from Arecibo with the 2004 Sumatra earthquake. They suggested that gravity waves launched by the tsunami were imperfectly ducted for long distances. The energy that

<sup>1</sup>Department of Physical Sciences, Embry-Riddle Aeronautical University, Daytona Beach, Florida, USA.

<sup>2</sup>Department of Earth and Space Sciences and Institute of Geophysics and Planetary Physics, University of California, Los Angeles, California, USA.

<sup>3</sup>Space Science Applications Laboratory, The Aerospace Corporation, Los Angeles, California, USA.

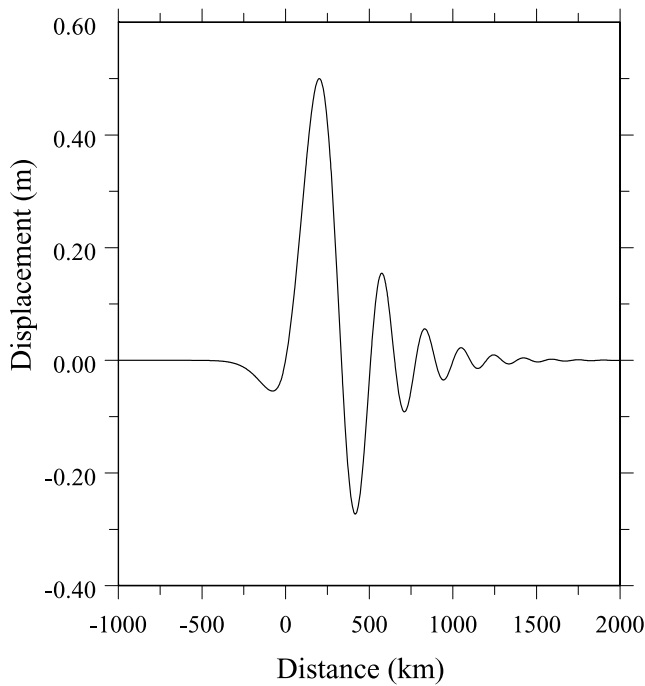


**Figure 1a.** Surface displacement ( $Z$ ) calculated using equation (1) for a maximum displacement of 0.50 m.

leaked into the ionosphere ultimately triggered instabilities, spread-F, and ionospheric turbulence.

[6] *Occhipinti et al.* [2006] coupled a 3-D model of earthquake-driven ocean disturbances with a 1-D model of atmospheric wave propagation and a simple 1-D ionospheric response model. The simulated ionospheric signature induced by the 2004 Sumatra earthquake was compared with TEC measurements from Jason-1 and Topex-Poseidon satellite altimeters. The overall agreement between model and measurements was good, with TEC perturbations of  $\sim 5$  TECU, or 10% of the undisturbed TEC value. However, because of the neglect of wave damping, the simulated disturbance speed in the neutral atmosphere was unrealistically large, with vertical and horizontal wind perturbations of  $\sim 600$  m s $^{-1}$ . More recently, *Occhipinti et al.* [2008] simulated the effects of different latitudes and wave propagation directions on the ionospheric response, but they also neglected the effects of wave damping.

[7] The atmospheric gravity wave model used by *Occhipinti et al.* [2006] neglected several important physical processes that would otherwise significantly influence the ionospheric response to the tsunami. These include the damping associated with molecular viscosity and thermal conduction; the damping associated with ion drag; the filtering effect of background mean winds; and the Coriolis force. In this paper we address these deficiencies by using a full-wave model that accounts for the processes mentioned above, as well as the eddy diffusion of heat and momentum in the upper mesosphere. This model and its application to the propagation of a tsunami signature through the atmosphere is described in section 2a. The mean and perturbation ionospheric models are described in section 2b. Results are

discussed in section 3, followed by a discussion and conclusions in sections 4 and 5, respectively.

## 2. Theory and Gravity Wave Model

[8] The sea surface displacements measured by Jason-1 and Topex-Poseidon [not shown], as reported by *Occhipinti et al.* [2006], suggest a dominant horizontal-scale size of 400 km with an amplitude of  $\sim 0.5$  m. Combined with the shallow water phase speed of  $\sim 200$  m/s this implies a dominant wave period of 33 min. The period, wavelength and phase speed of the tsunami surface wave are characteristic of medium-scale gravity waves [*Georges*, 1968], and suggest that efficient generation of gravity waves should occur [*Hines*, 1972].

[9] We use an approach described by *Peltier and Hines* [1976] to model the propagation of a tsunami-generated gravity wave packet. The initial ( $t = 0$ ) displacement  $Z$  at the sea surface ( $z = 0$ ) is prescribed by

$$Z(x, z = 0, t = 0) = A \left\{ Ai(-x + 1) \frac{x}{2} \exp[-(x - 2)/2] \right\} \quad (1)$$

where  $Ai$  is the Airy function, and  $x$  is the horizontal position in units of 100 km. The amplitude of the forcing is  $A$  (in meters).

[10] The Fourier transform of equation (1) provides the wavenumber ( $k$ ) spectrum of the forcing

$$\hat{Z}(k, 0, 0) = \frac{1}{2\pi} \int_{-\infty}^{\infty} Z(x, 0, 0) e^{ikx} dx \quad (2)$$

Long wavelength waves on the ocean surface are non-dispersive and propagate with the shallow water phase speed  $c = \sqrt{gh}$ , where  $g$  is the gravitational acceleration and  $h$  is the ocean depth [*Lighthill*, 1978]. We assume an ocean depth of  $\sim 4$  km, and the tsunami is taken to propagate with  $c = -200$  m/s. This implies that for every value of  $k$  in the spectrum defined by equation (2) there is a corresponding wave frequency,  $\omega = -200k$ .

[11] The full-wave model is run for each  $\omega - k$  pair in the spectrum. The vertical velocity spectrum is then calculated as

$$\hat{W}(k, 0, 0) = i\omega \hat{Z}(k, 0, 0) = -i200k \hat{Z}(k, 0, 0) \quad (3)$$

A discrete Fourier transform is used to evaluate the surface displacement ( $\hat{Z}$ ) and its vertical velocity spectrum ( $\hat{W}$ ) (see Figures 1a and 1b, respectively). The surface displacement (Figure 1a) is characterized by a rapid rise in amplitude followed by several trailing waves of diminishing amplitude. The vertical velocity spectrum (Figure 1b) has peaks at  $\pm 400$  km, which combined with a phase speed of 200 m/s corresponds to a dominant period of 33 min.

[12] Our full-wave model is used to propagate each wave component of the discretized spectrum through the atmosphere. The linear, steady-state model solves for temperature, pressure and the velocity perturbations by solving the Navier-Stokes equations subject to boundary conditions. The model includes height-dependent mean temperature, winds, and the eddy and molecular diffusion of heat and

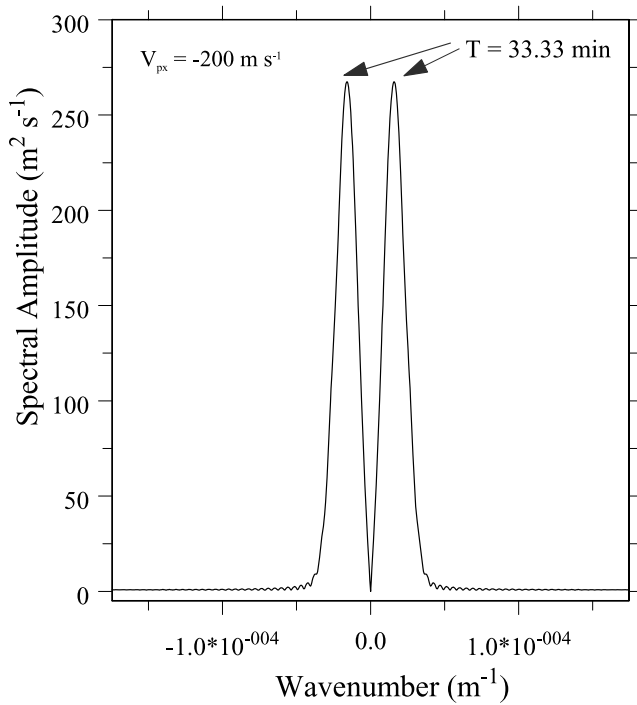


**Figure 1b.** Vertical velocity spectrum ( $\hat{W}$ ) calculated using equation (3).

momentum, ion drag, and the Coriolis force [Hickey *et al.*, 2001; Walterscheid and Hickey, 2001; Schubert *et al.*, 2005]. A wave is forced at the lower boundary ( $z = 0$ ) by specifying the vertical velocity. Denoting the full-wave model normalized output as  $\psi'_j(\omega, k, z)$ , where subscript  $j$  signifies temperature, pressure, or velocity, the response to lower boundary forcing is

$$\Psi'_j(x + vt, z) = \frac{1}{2\pi} \int_{-\infty}^{\infty} \hat{W}(k, 0, 0) \psi'_j(\omega, k, z) e^{-ik(x+vt)} dk \quad (4)$$

Equation (4) was implemented by forcing every wave to have a vertical velocity of 1 m/s at the lower boundary ( $w'(\omega, k, 0) = 1$  m/s). The product  $\hat{W}(k, 0, 0) \psi'_j(\omega, k, z) \Delta k$  represents the wavenumber-dependent perturbation. As discussed by Peltier and Hines [1976], many of the waves in the spectrum are evanescent and will not propagate very far in the atmosphere. Hence the spectrum is truncated to include only propagating waves. The minimum period was 3.0 min and corresponded to a minimum horizontal wavelength of 36 km. Equation (4) was solved for 800 waves (400 positive  $k$  and 400 negative  $k$ ) in the spectrum based on values of  $x$  ranging from  $-1000$  km to  $+14400$  km (so that the bandwidth  $\delta k = 4.36 \times 10^{-7} \text{ m}^{-1}$ ), and provided good spectral resolution for all the simulations.

[13] The individual wave components of the spectrum were calculated using a full-wave model. This model has been used to study acoustic wave [Hickey *et al.*, 2001; Schubert *et al.*, 2005] and gravity wave [Hickey *et al.*, 1997; Walterscheid and Hickey, 2001] propagation and dissipation in the terrestrial atmosphere. It has also been used to generate a spectrum of waves for time-dependent modeling

of the airglow response to gravity wave packets [Hickey *et al.*, 2000; Huang and Hickey, 2008]. The model solves the steady-state, linearized Navier-Stokes equations subject to boundary conditions for a single monochromatic wave of the form  $\exp i(\omega t - kx - ly)$ , where  $x$  and  $y$  are horizontal coordinates in the meridional and zonal direction, respectively, with corresponding horizontal wavenumbers  $k$  and  $l$ ,  $t$  is time, and  $\omega$  is the wave angular frequency. The resulting set of finite difference equations are solved using the tridiagonal algorithm described by Bruce *et al.* [1953] and Lindzen and Kuo [1969]. The model provides the magnitude and phase of the perturbation horizontal and vertical velocity components ( $u'$ ,  $v'$ , and  $w'$ ), the perturbation temperature ( $T'$ ), and the perturbation pressure ( $p'$ ) as a function of altitude.

[14] Our previous full-wave model simulations employed either a solid-surface lower boundary condition (with  $w' = 0$ ), or employed a deep lower sponge layer for which the wave solutions were independent of the lower boundary condition. Here, through a modified boundary condition, we force the wave vertical velocity at the ground lower boundary. For all simulations the upper boundary is set at 1000 km altitude and the vertical resolution is about 7 m. The molecular dissipation and Rayleigh sponge layer strongly inhibits any downward reflected waves from the upper boundary.

### 3. Electron-Ion Response Model

[15] The mean, undisturbed electron number densities are modeled by a Chapman layer having an F2 peak at 300-km altitude with a maximum number density of  $(N_m F_2) 10^{12} \text{ m}^{-3}$ , and with an E-layer peak at 105 km altitude and a number density of  $1.25 \times 10^7 \text{ m}^{-3}$ . The total electron content (TEC) was calculated by integrating the electron density over altitude. Its undisturbed value was  $\sim 17$  TECU, where 1 TECU =  $10^{16}$  electrons  $\text{m}^{-2}$ . More details of this and the calculation of the undisturbed ion number densities is provided in Appendix A.

[16] The modeled electron-ion response to a linear gravity wave includes the effects of dynamics and chemistry. The solution procedure is similar to that previously used to model the effect of gravity waves on minor species fluctuations and related airglow emissions in the mesopause region [Walterscheid *et al.*, 1987; Hickey, 1988]. The linearized perturbation ion continuity equations for  $\text{O}^+$ ,  $\text{O}_2^+$ ,  $\text{N}_2^+$  and  $\text{NO}^+$  are

$$i\omega n'_j + w'_j \frac{d\bar{n}_j}{dz} + \bar{n}_j \nabla \cdot \mathbf{v}'_j = P'_j - \bar{n}_j L'_j - n'_j \bar{L}_j \quad (5)$$

All terms in the above equation, including the perturbation chemical terms and the ion velocity calculation, are described in Appendix A. Altitude profiles of the undisturbed electron and ion number densities are given in Figure A1.

### 4. Undisturbed Mean Atmosphere

[17] The mean undisturbed atmosphere is defined using the MSIS-90 model [Hedin, 1991] for conditions prevailing at the equator at the time of the Sumatra earthquake, for a

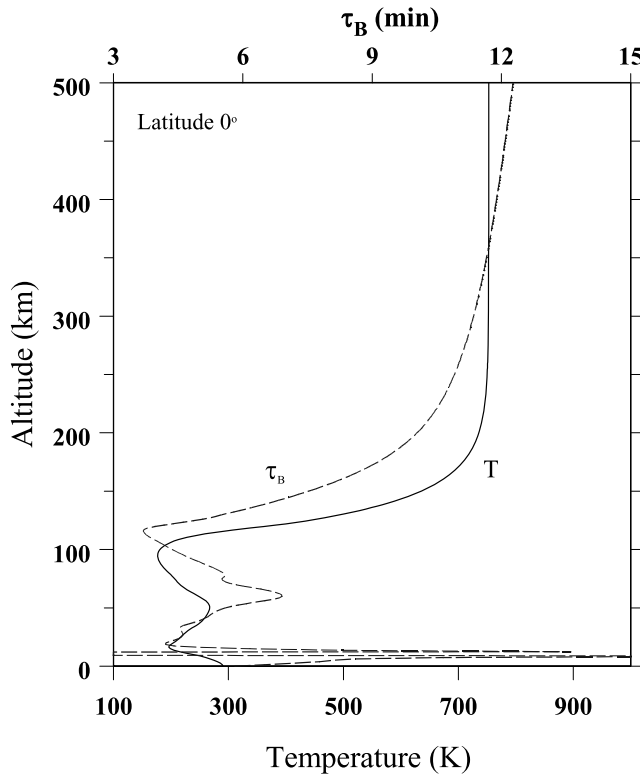


**Figure 2.** Mean temperature and Brunt-Väisälä period used in the simulations.

latitude and longitude of  $0^\circ$  and  $85^\circ$ , respectively, and for a UT of 0300 hours on 26 December. The solar  $F_{10.7}$  index and its 81-day mean are 88.7 and 102.8, respectively. The geomagnetic index  $a_p = 12$ . Winds (when included) are described by the HWM93 model [Hedin *et al.*, 1996] using these same inputs.

[18] Figure 2 shows the altitude profiles of mean temperature (lower  $x$  axis) and the Brunt-Väisälä period (upper  $x$  axis) used in this study. The temperature exhibits the usual variation with altitude, and reaches an exospheric temperature of  $\sim 753$  K at high altitudes. The altitude variation of the Brunt-Väisälä period indicates that waves up to about 4 min periods will be evanescent throughout the atmosphere. Above 100 km altitude  $\tau_B$  increases with increasing altitude, which will lead to the removal of progressively more of the high-frequency waves during the upward propagation of a spectrum of waves (or a wave packet). Near the F-region peak,  $\tau_B$  has the value of about 12 min, so we expect waves of period longer than this to dominate the F-region response to an upward-propagating wave packet.

[19] Figure 3 shows profiles of the mean winds used in the simulations. The meridional wind (solid line) is typically small ( $<10$  m/s) below 100 km altitude. Above that it varies slightly, and then decreases to about 45 m/s in the northward direction near 165 km altitude, after which it smoothly decreases to about 17 m/s northward by 500 km altitude. The zonal wind (dashed line) is about 40 m/s eastward near the stratopause (50 km), and it decreases to 10 m/s westward at about 100 km altitude. At greater heights it increases in the eastward direction, reaching a maximum eastward speed of about 75 m/s near 240 km altitude. At

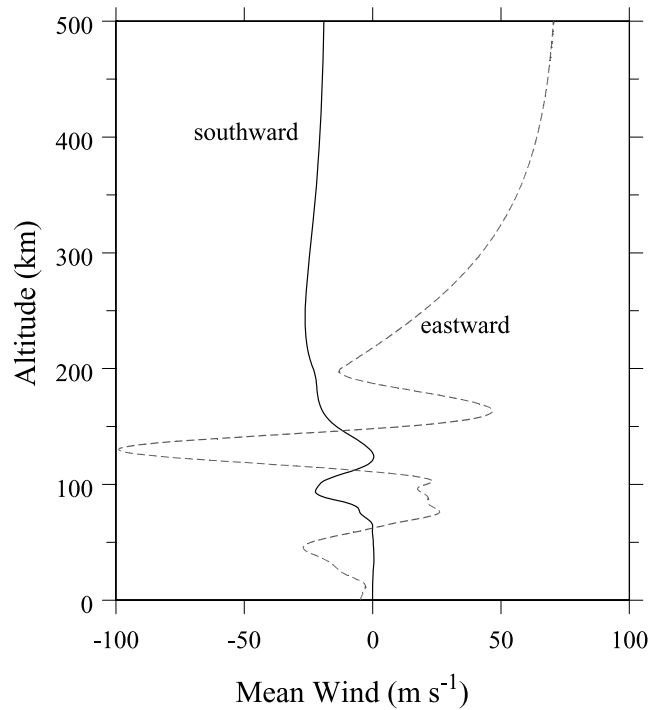


**Figure 3.** Mean horizontal winds [Hedin *et al.*, 1996] used in the simulations.

greater heights it smoothly decreases, reaching about 56 m/s eastward at 500 km altitude.

[20] Figure 4 shows altitude profiles of the kinematic viscosity. The nominal profile (solid line) has an eddy diffusion component that maximizes at 90 km altitude with a value of  $100 \text{ m}^2/\text{s}$ . At greater heights the molecular

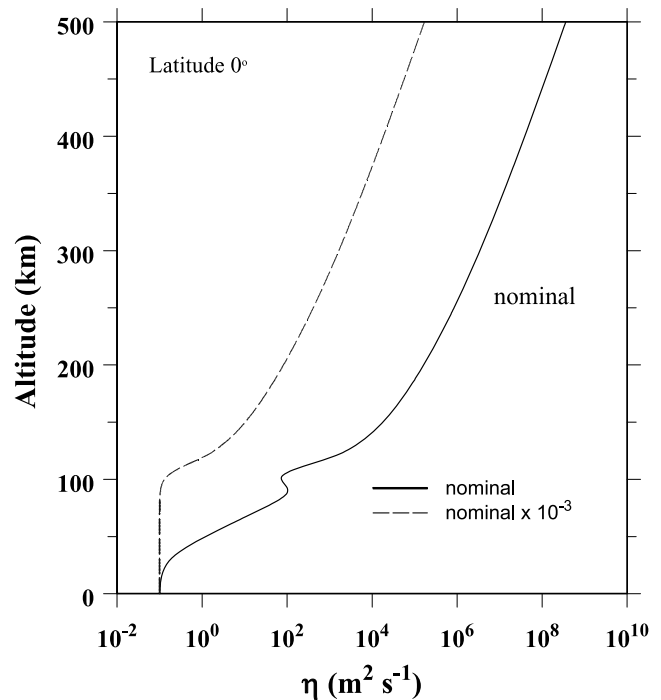


**Figure 4.** Nominal (solid line) and quasi-adiabatic (dashed line) kinematic viscosity used in the model.



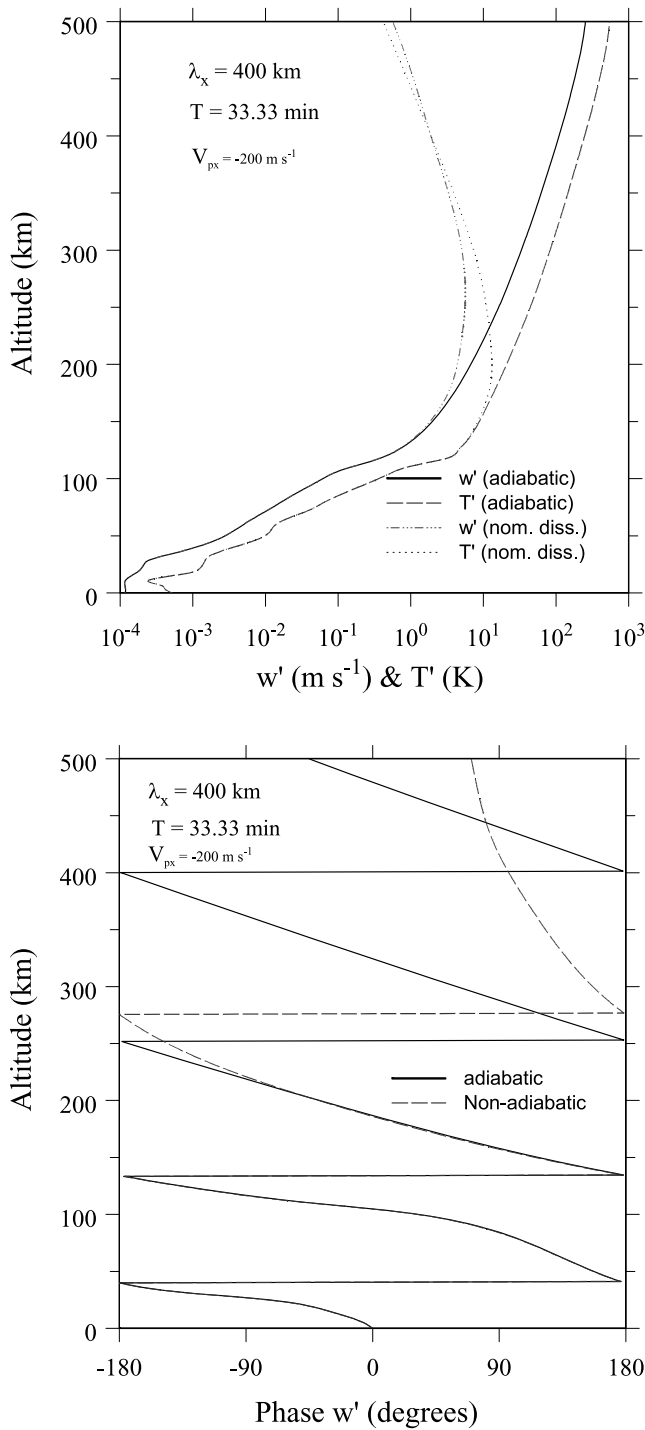


**Figure 5.** (a) Amplitude and (b) phase for 400-km wave and for nominal and reduced dissipation (see legends). The vertical wavelength (b) is  $\sim 100$  km at low altitudes and exceeds 150 km at higher altitudes.

viscosity dominates, and it increases smoothly with increasing altitude to a value of  $10^8$  m<sup>2</sup>/s at 500 km. To help facilitate comparison with the simulations of *Occhipinti et al.* [2006] we also consider the effect of reducing the kinematic viscosity by a factor of 1000 from its nominal value (dashed line) and using a constant eddy diffusivity of

$0.1$  m<sup>2</sup>/s (which we refer to as “quasi-adiabatic” in the model simulations). It is clear from Figure 4 that the nominal dissipation rate near 150 km altitude is not achieved until much greater altitudes ( $\sim 500$  km) for the quasi-adiabatic simulations. Hence we expect a wave spectrum to propagate to much greater altitudes in a quasi-adiabatic atmosphere before being severely dissipated.

## 5. Results

### 5.1. Results for Dominant Wave

[21] The dominant wave in the spectrum of Figure 1b has a horizontal wavelength of 400 km and a period of  $\sim 33.3$  min. This wave is forced at the lower boundary of the full-wave model with a vertical velocity amplitude of  $1.17 \times 10^{-4}$  m s<sup>-1</sup> (its spectral amplitude multiplied by the bandwidth). The altitude variation of wave amplitude and phase for the 400 km wave is shown in Figures 5a and 5b, respectively. For this simulation only the Coriolis force and ion drag were not included. In the atmosphere with nominal viscosity the wave amplitude (Figure 5a) grows with increasing altitude up to about 200 km altitude, where the maximum temperature and vertical velocity amplitudes reach values of about 10 K and 7 m/s, respectively. At greater heights the wave amplitude diminishes because of viscous dissipation. In the quasi-adiabatic atmosphere, the wave amplitude continues to increase at altitudes greater than 200 km. At 500 km altitude the perturbation temperature and vertical velocity amplitudes reach values of about 700 K and 200 m/s, respectively. The phase variation of the perturbation vertical velocity is shown in Figure 5b. Up to about 200 km altitude the vertical wavelength of this wave is approximately 100 to 120 km. In the quasi-adiabatic atmosphere (solid line) the vertical wavelength increases slightly at greater heights as a consequence of the increase of  $\tau_B$ . The inclusion of realistic dissipation (dashed line) causes a dramatic increase of the vertical wavelength at great heights, and the wave is approaching evanescence by 500 km altitude.

[22] Simulations for the 400 km wave were repeated with ion drag and Coriolis force included and for eastward and northward phase propagation in an atmosphere of nominal viscosity. The new amplitudes and phases obtained for  $w'$  and  $T'$  were similar to those shown in Figure 5 and so are not shown here (although we note that the amplitudes were slightly diminished for the eastward-propagating wave because of the increased ion drag). Altitude profiles of the perturbation  $O^+$  velocity components are shown in Figure 6a. These results show the dramatic effect of gravity wave propagation direction on the ion velocity. The largest ion velocity response occurs for the meridional velocity component for northward gravity wave propagation. At 200 km altitude it is  $\sim 15$  m/s. For the eastward-propagating gravity wave the meridional ion velocity response was less than  $10^{-4}$  m/s. For this wave the largest ion velocity component was the vertical velocity, but it decreased rapidly with increasing altitude and was only about  $10^{-2}$  m/s near 300-km altitude. Above  $\sim 150$  km altitude the zonal ion velocity response was approximately equal for the eastward and northward-propagating gravity waves. The vertical velocity response for the northward-propagating gravity wave was small ( $< 10^{-4}$  m/s) in the F-region ionosphere.

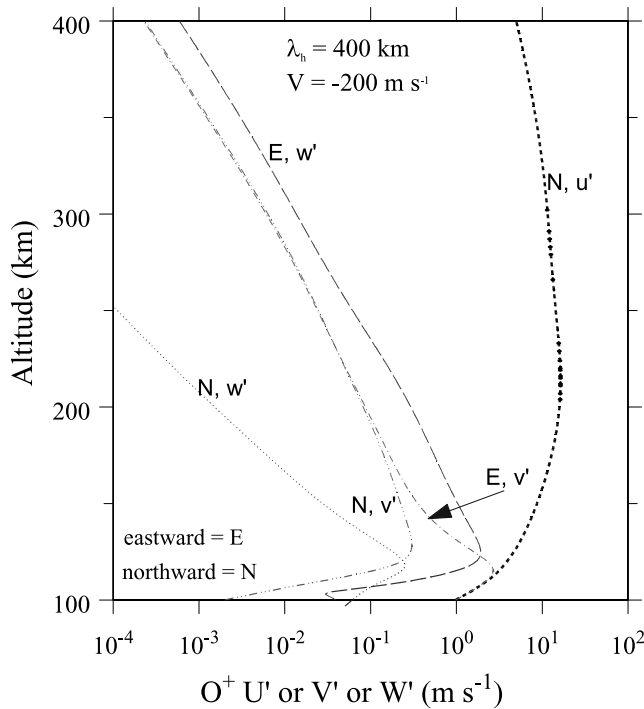


**Figure 6a.**  $O^+$  ion velocities calculated from equation (A5) for northward- and eastward-propagating waves at the equator. Ion velocities are small for eastward-propagating waves.

[23] The electron density response to these two gravity waves, and also to a third gravity wave propagating northward in a quasi-adiabatic atmosphere, is shown in Figure 6b. Below 200 km altitude the electron response is greatest for the eastward-propagating gravity wave. At greater heights the response is greater for the northward-propagating gravity wave, especially so for the quasi-adiabatic case. At 300-km altitude the electron density response is  $\sim 10^{-2}$  % for the eastward-propagating wave, and 7 % and 70% for the northward-propagating waves in the nominal and quasi-adiabatic atmospheres, respectively. This large anisotropy is explained as follows. The ion response is dominated by the ion velocity divergence. For the northward-propagating wave the ion velocity divergence is dominated by the horizontal velocity gradient, which is large because the meridional velocity fluctuation amplitude is large (see Figure 6a). For the eastward-propagating wave the ion velocity is dominated by the vertical velocity gradient (the zonal ion velocity is very small), but the vertical velocity is also small near the  $F_2$  peak (see Figure 6a).

## 5.2. Spectral Results

[24] In this section we present results obtained for the spectral model with 800 waves to evaluate equation (4). Initially we compare results obtained for propagation in a quasi-adiabatic atmosphere with those obtained for propagation in an atmosphere with realistic viscosity.

[25] The horizontal and vertical perturbation velocities obtained for northward propagation in a quasi-adiabatic atmosphere are shown in Figures 7a and 7b, respectively. In Figures 7a and 7b propagation is to the left. The gravity wave phase fronts slope upward to the left, indicative of

downward phase propagation accompanying upward energy propagation. The horizontal perturbation velocity (Figure 7a) grows with increasing altitude, reaching a maximum amplitude of  $\sim 6600$  m/s near 550 km altitude. At 300-km altitude the horizontal perturbation velocity is  $\sim 1160$  m/s. The maximum disturbance amplitudes occur at horizontal locations ( $0 < x < 600$  km) where the surface displacement (Figure 1a) maximizes. The perturbation vertical velocity (Figure 7b) also grows with increasing altitude, reaching a maximum amplitude of  $\sim 2200$  m/s near 550 km altitude. At 300-km altitude the maximum vertical wind velocity is  $\sim 300$  m/s.

[26] The horizontal and vertical perturbation velocities obtained for northward propagation in an atmosphere with realistic viscosity are shown in Figures 8a and 8b, respectively. As before the phase fronts slope upward to the left, but the slope becomes steeper with increasing height (the vertical wavelength increases) because of the increased kinematic viscosity and dissipation rate at higher altitudes. The horizontal perturbation velocity initially increases with increasing altitude, but viscous dissipation causes a decrease of wave amplitude at heights above  $\sim 300$  km. At 300 km the maximum horizontal velocity perturbation is  $\sim 100$  m/s, which is more than an order of magnitude smaller than the quasi-adiabatic result (Figure 7a). The vertical perturbation velocity (Figure 8b) displays similar characteristics to the horizontal perturbation velocity, with a maximum value of  $\sim 30$  m/s near 300-km altitude.

[27] The resulting electron number density perturbations for northward propagation are shown in Figure 9. For propagation in a quasi-adiabatic atmosphere (Figure 9a) the electron density perturbations maximize near 400 km altitude (that is, above the  $F_2$  peak) with values near  $9 \times$

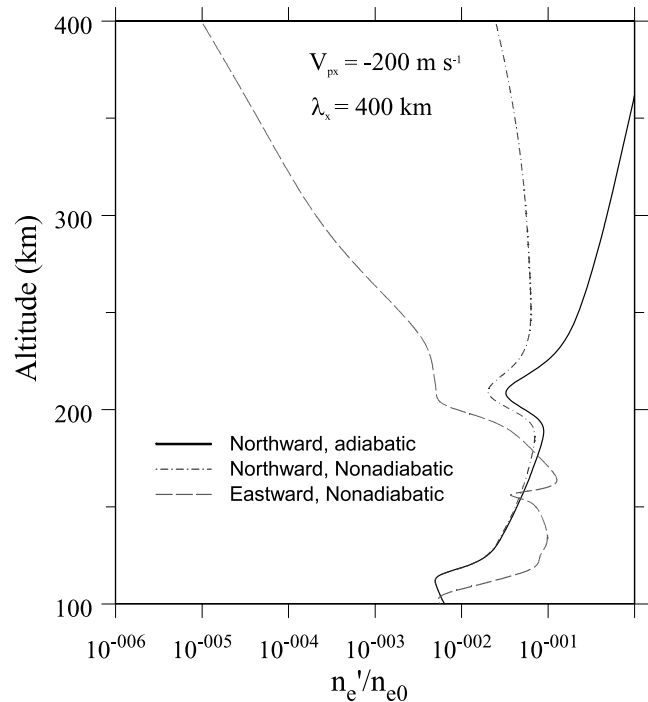


**Figure 6b.** Electron density fluctuation amplitudes calculated from equation (A7). They are small for eastward-propagating waves at the equator.

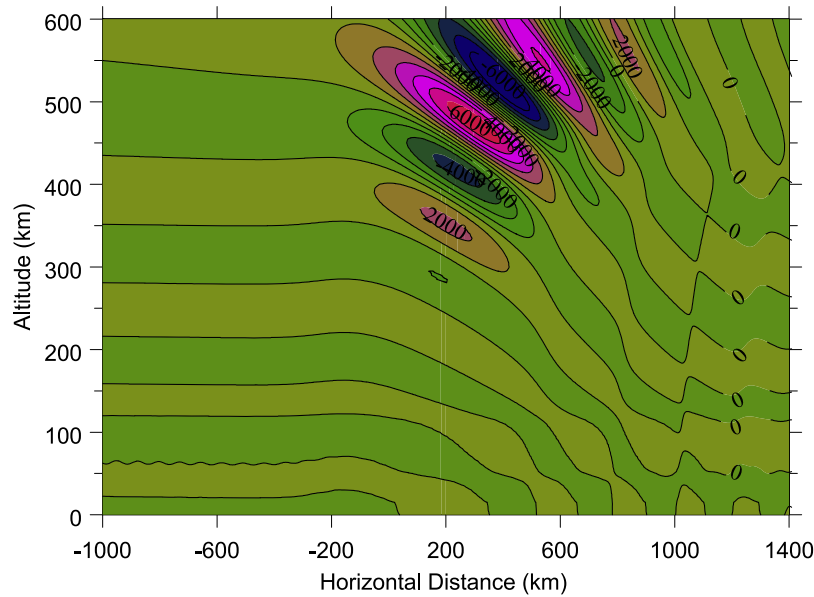


**Figure 7a.** Horizontal velocity perturbation for northward propagation in a quasi-adiabatic atmosphere. The maximum wind perturbation is  $\sim 1160$  m/s near 300-km altitude.

$10^{12} \text{ m}^{-3}$ . Additionally, at horizontal locations near 200 km, strong vertical structure occurs in the electron density perturbations. For propagation in an atmosphere with realistic viscosity (Figure 9b) the phase fronts are more vertical because of the strong dissipation, while the vertical structure reveals a disturbance primarily concentrated over a half vertical wavelength. The maximum electron density fluctuations occur at the F2 peak (300-km altitude), with maximum values of  $\sim 6 \times 10^{11} \text{ m}^{-3}$  near  $x = 200$  km.

[28] The electron density fluctuations for eastward wave propagation are shown in Figure 10. For propagation in a quasi-adiabatic atmosphere (Figure 10a) the electron density fluctuations maximize just below 300-km altitude, with a maximum near  $1.5 \times 10^{10} \text{ m}^{-3}$ . The fluctuation amplitudes

are almost three orders of magnitude smaller than those for northward propagation because the ion velocity response is small for zonal propagation (see Figure 3a). For propagation in an atmosphere with realistic viscosity (Figure 10b) the electron density fluctuations are half as large as those with reduced dissipation. The maximum fluctuation amplitude is  $\sim 7 \times 10^9 \text{ m}^{-3}$  near 240 km altitude. The vertical extent of the electron density disturbance is small in this case ( $\sim 50$  km) and is confined primarily to the lower F region.

[29] The electron density fluctuations for wave propagation in an atmosphere with mean winds and with realistic viscosity are shown in Figure 11. For northward propagation (Figure 11a) the maximum fluctuation amplitude is  $\sim 3 \times 10^{11} \text{ m}^{-3}$ , which is about half that of the corresponding

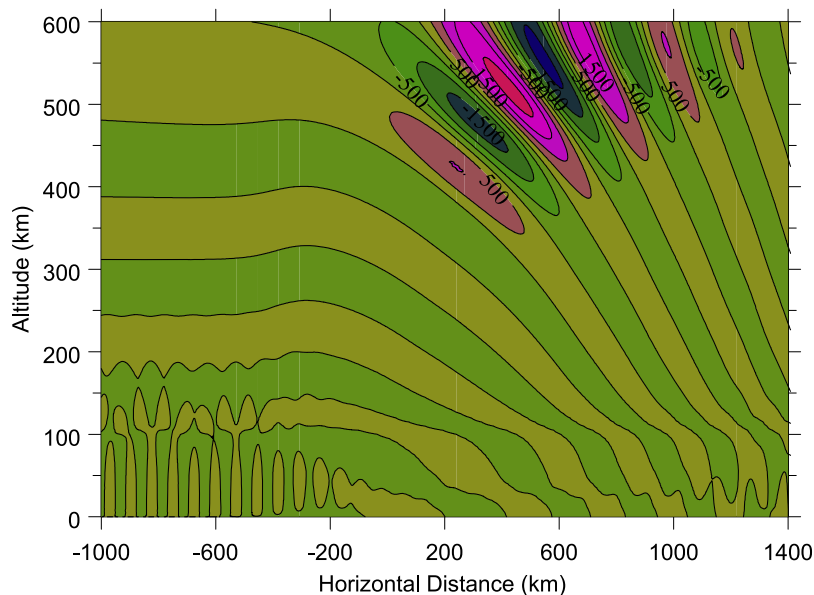


**Figure 7b.** Vertical velocity perturbation for northward propagation in a quasi-adiabatic atmosphere. The maximum wind perturbation is  $\sim 300$  m/s near 300-km altitude.



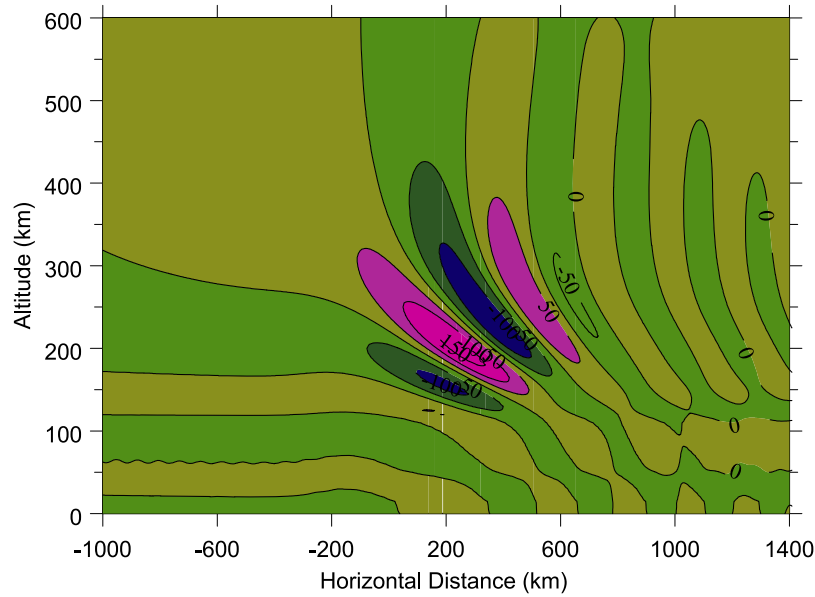


**Figure 8a.** Horizontal velocity perturbation for northward propagation in a nonadiabatic atmosphere. The maximum wind perturbation is  $\sim 100$  m/s near 300-km altitude.

windless case. For eastward propagation (Figure 11b) the maximum fluctuation amplitude is  $\sim 1 \times 10^9 \text{ m}^{-3}$ , which is several times smaller than the corresponding windless case. For both directions of wave propagation the mean winds reduce the electron density response, but the largest effect of the winds is for eastward propagation.

[30] The fluctuations in the total electron content (TEC), obtained by integrating over altitude the electron densities previously presented in Figures 9, 10, and 11, are shown in Figure 12. The TEC fluctuations for northward wave propagation (Figure 12a) are largest for the quasi-adiabatic and windless case, with a maximum (negative) amplitude of 15 TECU (where  $1 \text{ TECU} = 10^{16} \text{ m}^{-3}$ ). The mean,

undisturbed total electron content is 17 TECU, and hence the TEC fluctuations are  $\sim 90\%$  of the mean in this case. The inclusion of realistic viscosity reduces the magnitude of the TEC fluctuations to  $\sim 5$  TECU (30% of the mean), while the further inclusion of mean winds reduces the TEC fluctuations to  $\sim 3$  TECU (less than 20% of the mean). In the latter case the initial arrival of the disturbance exhibits the largest fluctuation amplitude, whereas in the other, windless cases the initial arrival of the disturbance is followed by a larger fluctuation.

[31] The TEC fluctuations for eastward wave propagation are shown in Figure 12b. The TEC response for eastward wave propagation is significantly smaller (by a factor of

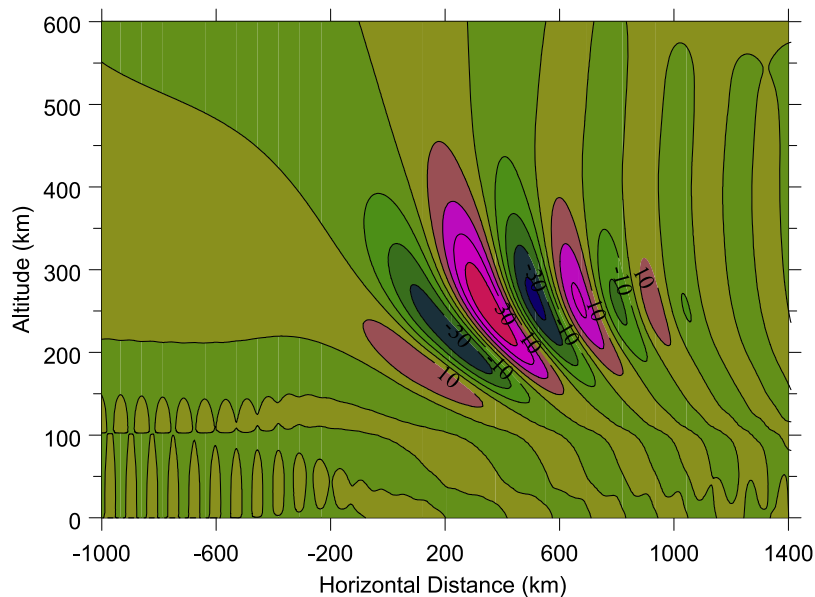


**Figure 8b.** Vertical velocity perturbation for northward propagation in a nonadiabatic atmosphere. The maximum wind perturbation is  $\sim 30$  m/s near 300-km altitude.

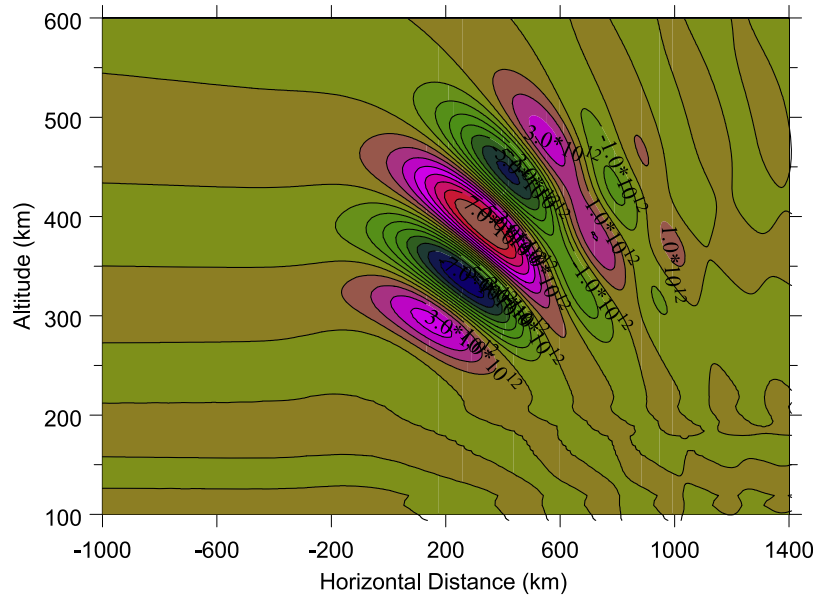


**Figure 9a.** Electron density perturbations for northward propagation without dissipation. The maximum contour value is  $9 \times 10^{12} \text{ m}^{-3}$ .

$\sim 50$ ) than for northward propagation in all cases considered. The largest response for eastward propagation occurs for the quasi-adiabatic case, and is characterized by a single positive pulse of magnitude  $\sim 0.18$  TECU (or 1% of the mean) near  $x = 200$  km, followed by a slow decrease to zero with several smaller superimposed undulations. The initial response for the case of realistic viscosity resembles a sinusoidal variation with a negative phase followed by a decay to zero over three or four cycles. The maximum amplitude in this case is  $\sim 0.03$  TECU. With the further inclusion of mean winds the TEC response is less than about one third this value, but the undulations are almost in

phase with those of the previous case (realistic viscosity and no winds).

## 6. Discussion

[32] In order to help facilitate an assessment of the assumptions used in the simulations of *Occhipinti et al.* [2006] we have performed simulations at the equator. In the case of zonal wave propagation the ion and electron response is then extremely small. The response at higher latitudes where the magnetic field is not horizontal would give a much larger ion-electron response through the nonzero cross product of the zonal wind perturbation with

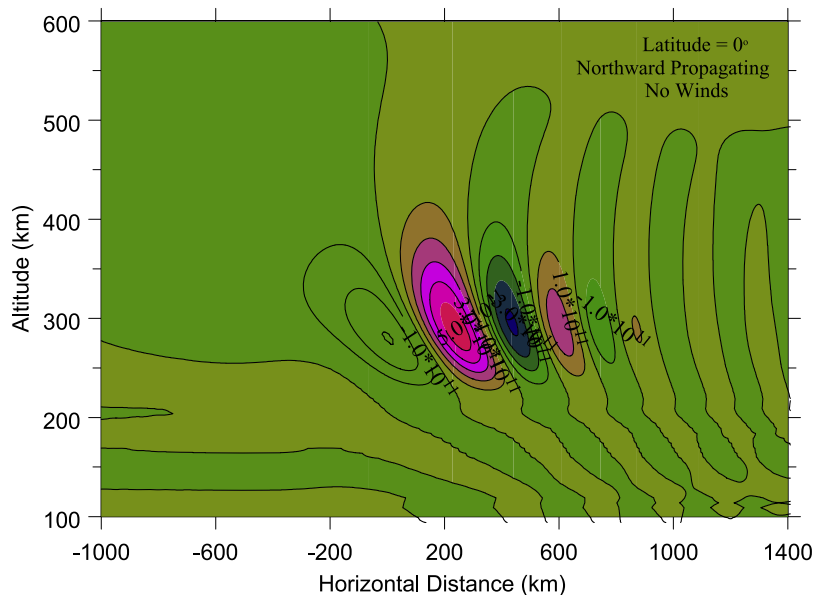


**Figure 9b.** Electron density perturbations for northward propagation without mean winds. The maximum contour value is  $6 \times 10^{11} \text{ m}^{-3}$ .

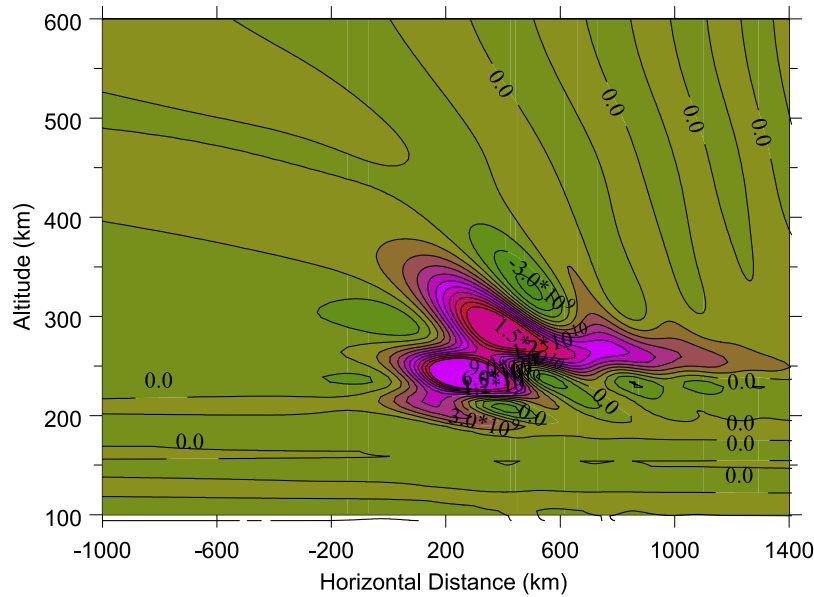


**Figure 10a.** Electron density perturbations for eastward propagation without dissipation. The maximum contour value is  $1.5 \times 10^{10} \text{ m}^{-3}$ .

the magnetic field. Results obtained (but not shown) for the single dominant (400 km) wave in the spectrum verify this. More recent simulations by *Occhipinti et al.* [2008] have reconsidered the effect of a tsunami-driven gravity wave packet on the ionosphere for latitudes other than the equator, and shown that a strong sensitivity to latitude and to propagation direction exists.

[33] In this study we chose to model the electron density profile using a Chapman function. If specific events were to be modeled it would be better to use a measured electron density profile. However, for the present study this was not an important consideration because we were mainly interested in assessing the impact of certain specific physical

processes on the electron response. Additionally, because we have used a linear model the results obtained can be scaled accordingly using a different value of NmF2 or else using a different surface displacement amplitude for the tsunami.

[34] Our choice of tsunami parameters is intended to provide a plausible spectrum of gravity waves. The phase speed is based on an ocean depth of  $\sim 4$  km, for which the shallow water phase speed is  $\sim 200$  m/s. Deeper water supports faster waves. We investigated the effect of increasing the ocean depth by 20%, increasing the phase speed to 220 m/s. Results not shown indicate that for a nonisothermal atmosphere the faster waves are close to evanescence over

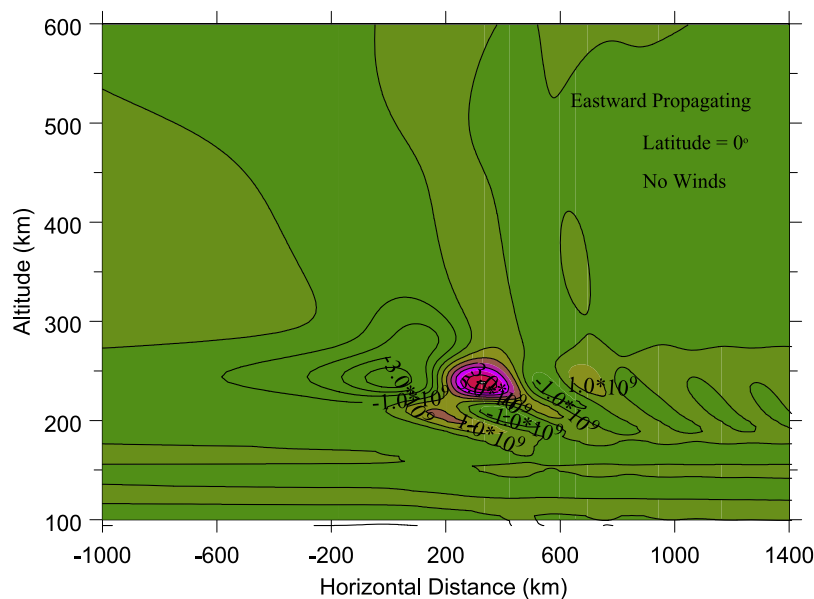


**Figure 10b.** Electron density perturbations for eastward propagation without mean winds. The maximum contour value is  $7 \times 10^9 \text{ m}^{-3}$ .

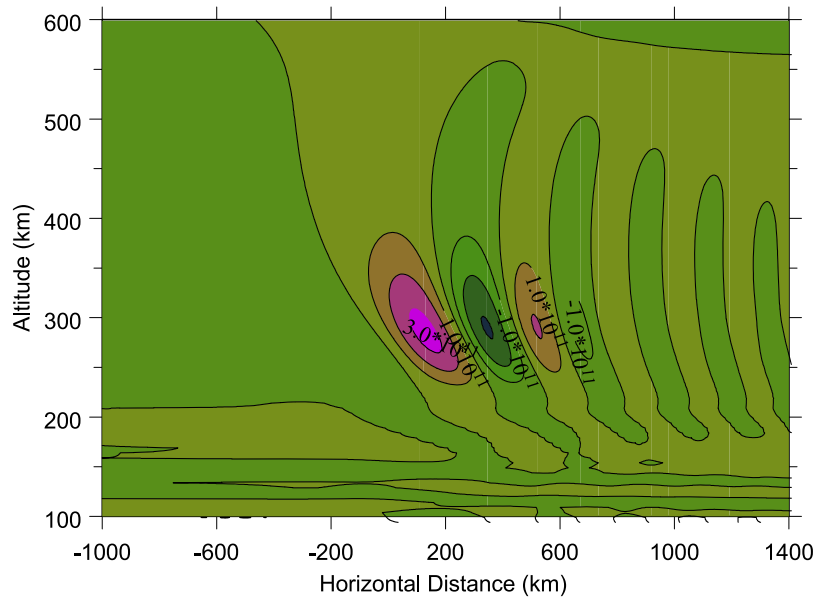


**Figure 11a.** Electron density perturbations for northward propagation including mean winds. The maximum contour value is  $3 \times 10^{11} \text{ m}^{-3}$ .

much of the mesosphere. The proximity to evanescence alters the aspect ratio  $u'/w'$ . It is smaller by a factor of  $\sim 3$  for the 220 m/s wave than for the 200 m/s wave. Consequently, the  $u'$  amplitudes for the 220 m/s wave are much smaller at all altitudes than for the 200 m/s wave. This in turn results in much smaller electron density perturbations for the faster wave since the effects of  $u'$  dominate near the equator. We note that in the case of an isothermal atmosphere the aspect ratios for the 200 m/s and 220 m/s waves are similar because they are never close to evanescence; thus they have comparable values of  $u'$  at all altitudes. This gives the result that the electron density fluctuations are also similar at all altitudes. Away from the equator where  $w'$  also influences

the ionospheric response the 200 m/s and 220 m/s waves should produce a similar response even in a nonisothermal atmosphere. Taken together, these findings suggest that for propagation in a realistic atmosphere the response at low latitudes will favor waves that are not too fast. Our analysis suggests that 200 m/s is close to an optimum speed. Hence at low latitudes, the ionospheric response to a tsunami should maximize in regions where the ocean depth is not too different from 4 km.

[35] Observations related to the Sumatra tsunami event reveal a range of possible wave periods. Spectral analysis of tide gauge measurements obtained from eight different sites (primarily in the Indian Ocean) reveal a range of periods

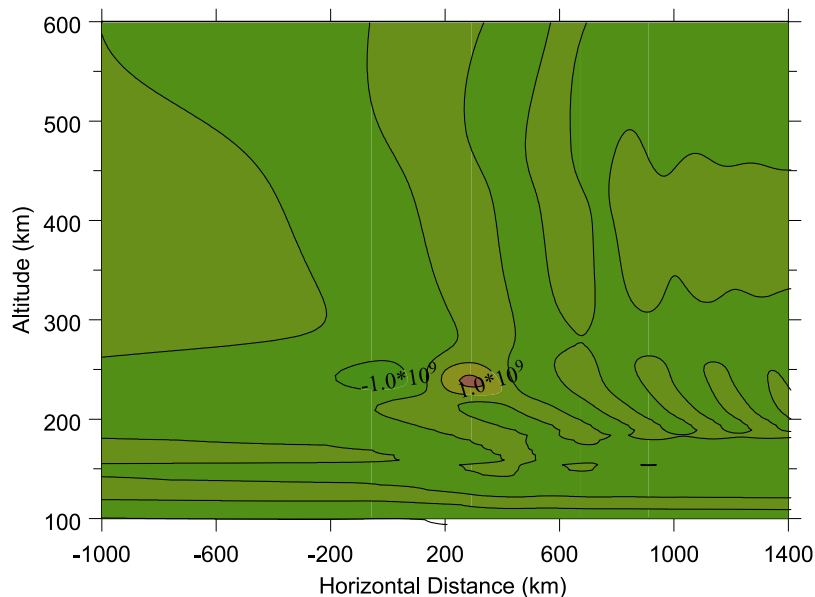


**Figure 11b.** Electron density perturbations for eastward propagation including mean winds. The maximum contour value is  $1 \times 10^9 \text{ m}^{-3}$ .

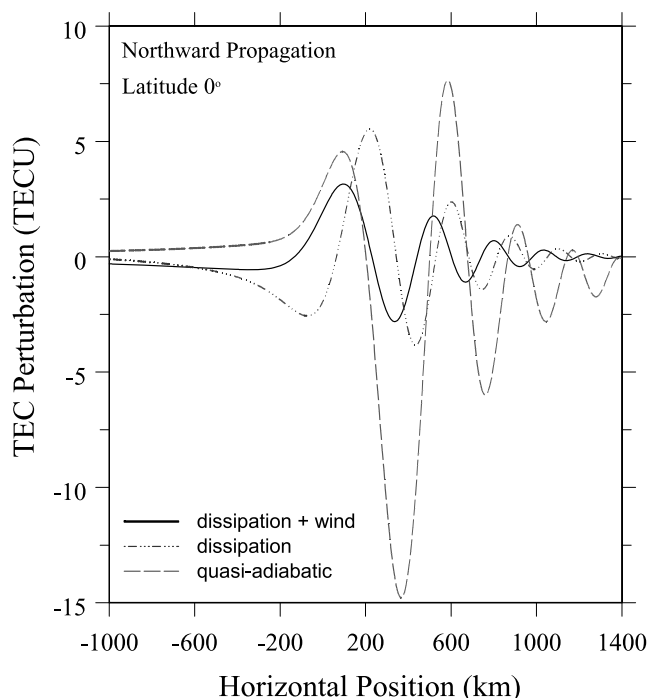


**Figure 12a.** TEC fluctuations for northward propagation.

varying from  $\sim 10$  to 60 min and a dominant period of  $\sim 40$  min [Abe, 2006]. Spectral analysis of tide gauge data encompassing a larger geographic area gave a range of wave periods varying from  $\sim 15$  min up to  $\sim 3$  hours [Rabinovich and Thomson, 2007]. GPS observations of ionospheric total electron content reveal TIDs of period  $\sim 20$  min [Liu et al., 2006]. Our choice of 33 min is certainly within the range of measured periods for this event. It differs from the value of 40 min reported by Abe [2006], but only by  $\sim 20\%$ , and so assuming a dominant period of 40 min would not have a significant impact on our conclusions.

[36] The primary wave parameters affecting the viscous dissipation of gravity waves are the horizontal phase speed and the vertical wavelength (which are directly related for most gravity waves). Ion drag dissipation depends strongly on wave period but it is only important for waves with periods of an hour or more. For the wave period of 33 min considered here and for zonal propagation at the equator (conditions for maximizing the effects of ion drag) we find that ion drag dissipation is far less important than viscosity in the damping of the waves. Our simulations have shown that the total wave field, which includes all waves in the spectrum and therefore includes a large range of wave periods, is not strongly affected by ion drag dissipation.

[37] Our full-wave model used in these simulations describes linear acoustic-gravity waves. A criterion for the onset of wave convective instability is  $u' > c$ , where  $u'$  is the horizontal wind perturbation and  $c$  is the horizontal phase speed [Orlanski and Bryan, 1969]. In our simulation results obtained with minimal molecular diffusion, the maximum value of  $u'$  at 300-km altitude was  $\sim 1160$  m/s, which is considerably greater than the 200 m/s phase speed. The amplitude was even greater at higher altitudes with reduced molecular diffusion. In our results obtained with the nom-

inal molecular diffusion, the maximum value of  $u'$  at 300-km altitude was  $\sim 100$  m/s, which is half the phase speed. Hence the linear assumption is valid. Note also that the maximum value of  $u'$  obtained with the nominal diffusion coefficients is much less than the sound speed ( $\sim 880$  m/s) in this region of the atmosphere.

[38] Although a tsunami-driven gravity wave packet may be observable through the traveling ionospheric disturbance (TID) it produces, there are other experimental methods that are also capable of detecting such disturbances. All-sky, image-intensified CCD camera systems are capable of revealing two-dimensional structure in the 6300-Å nightglow. All-sky airglow images can be obtained with a temporal resolution from 180 s [Kubota et al., 2001] up to several minutes [Mendillo et al., 1997; Martinis et al., 2006]. Spatial resolution is  $\sim 1$  km. Disturbances in the OI 6300-Å nightglow correlate well with TIDs because the emission is intimately related to the ion chemistry [Mendillo et al., 1997]. Observations of the 6300-Å nightglow have revealed gravity waves with phase speeds ranging from 50 m/s to several hundred m/s, and horizontal wavelengths ranging from a few hundred km up to  $\sim 5000$  km [Mendillo et al., 1997; Taylor et al., 1998; Kubota et al., 2001]. Fluctuation amplitudes of 20% to 30% for the 6300-Å nightglow appear to be quite common. The parameters of the gravity wave packet considered here are similar to those described in these previous observations, suggesting that observations of the 6300-Å nightglow would be useful in the detection of tsunami effects in the thermosphere.

## 7. Conclusions

[39] We have simulated the neutral atmosphere response, the electron density response, and the TEC response to a gravity wave packet propagating through the atmosphere

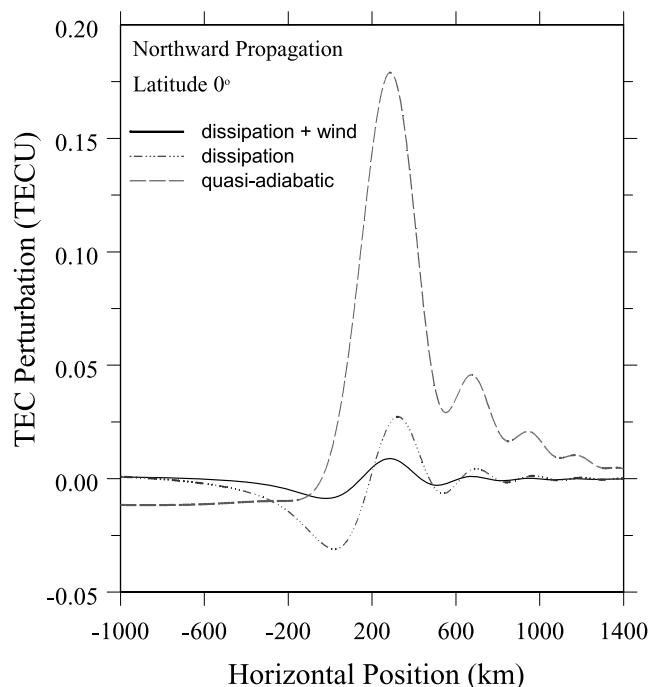


**Figure 12b.** TEC fluctuations for eastward propagation.



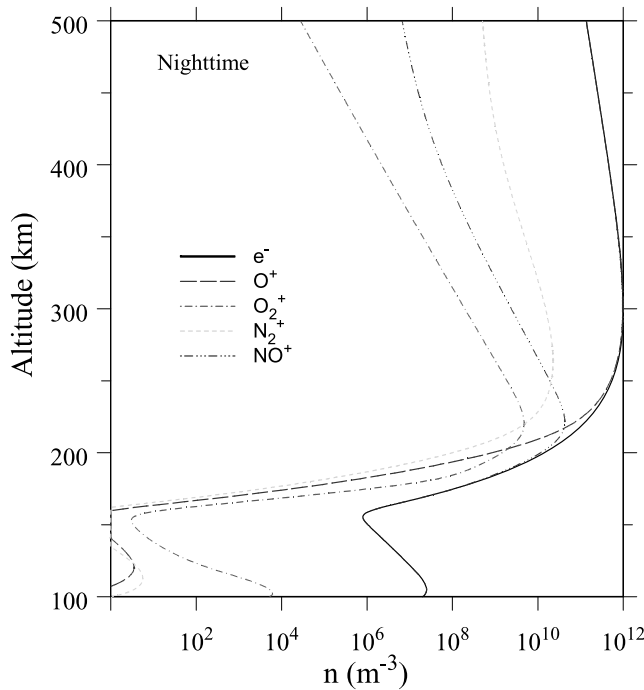


**Figure A1.** Undisturbed electron and ion densities calculated using equations (A1) and (A2), respectively.

under different conditions. The atmospheric response is unrealistically large for wave propagation under quasi-adiabatic conditions, with neutral wind perturbations of 100s of m/s and with the ionospheric response being  $\sim 100\%$  (both in number density and TEC). This case is similar to that considered by *Occhipinti et al.* [2008]. The neutral atmospheric response was an order of magnitude smaller for wave propagation in an atmosphere having realistic viscosity. Although the corresponding ionospheric response was also an order of magnitude smaller than before, the TEC response was only a factor of  $\sim 3$  smaller than before because of smaller cancellation effects in the vertical integration of the electron density. The ionospheric response for northward wave propagation was significantly greater (by a factor of  $\sim 50$ ) than for eastward wave propagation (at the equator). Mean winds also affected the neutral atmosphere and the ionospheric response, more so for eastward wave propagation because of the overall dominance of the zonal winds over the meridional winds. On the basis of an assumed surface displacement amplitude of 0.5 m, the most realistic of our simulations produce TEC fluctuations of  $\sim 3$  TECU and 0.02 TECU for northward and eastward wave propagation, respectively. While the response for northward wave propagation (which is about 20% of the mean) would be observable, it seems unlikely that the response for eastward propagation would be observable. This would impose limitations on the usefulness of ionospheric monitoring as a means to track or predict the arrival of tsunamis at very low latitudes. On the basis of our model simulations (at the equator), such an approach would seem feasible when tsunami propagation toward land is in the meridional direction, but not when it is in the zonal direction. More work is needed to study the ionospheric response to tsunamis propagating at midlatitudes.

[40] We have shown that damping by molecular diffusion (viscosity and thermal conductivity) and filtering by mean winds has a profound effect on gravity wave propagation in the thermosphere and also on the electron density perturbations they produce. The ion and electron response to a gravity wave are smaller for zonal wave propagation (for the low latitude considered here). Hence the net result is that electron density fluctuations and fluctuations in total electron content are almost two orders of magnitude larger for meridional wave propagation. In spite of the fact that these fluctuations are considerably smaller than those obtained by *Occhipinti et al.* [2006] (who neglected damping) the tsunami-generated waves are of sufficient amplitude to produce observable effects in the ionosphere. Additionally, it is noteworthy that in our simulations the maximum values of energy flux leaving the troposphere are about  $5 \times 10^{-4} \text{ W/m}^2$ , which would probably produce other interesting, short-term effects in the thermosphere.

## Appendix A

### A1. Ion Chemistry

[41] The ion chemistry is taken from *Schunk and Sojka* [1996] with some reaction rates taken from *Rees* [1989]. The following reactions are included in the model (Figure A1 and Tables A1 and A2).

[42] We note that some of these reactions depend on electron temperature rather than neutral temperature. We use the neutral temperature in all reactions. This is not a bad approximation here because it is the fluctuations in the rate constants associated with the waves, and hence the temperature fluctuations that are of primary importance. It is unlikely that the waves would drive significantly different temperature fluctuations in neutrals and electrons.

[43] The neutral species listed in the above tables were taken from the MSIS model except for NO. We modeled NO as a Gaussian profile with a maximum number density of  $10^{14} \text{ m}^{-3}$  at 115 km altitude with a full-width at half-maximum of  $\sim 42$  km. This is a good representative profile based on the published measurements of *Marsh et al.* [2004]. Our results are not very sensitive to this choice of NO because NO is important only in the E-region ionosphere where (in this study) the electron densities are very

**Table A1.** Chemical Reactions for Ions

	Ion Reaction	Rate ( $\text{cm}^3 \text{ s}^{-1}$ )
1	$\text{O}^+ + \text{N}_2 \rightarrow \text{NO}^+ + \text{N}$	$k_1 = 5 \times 10^{-13}$
2	$\text{O}^+ + \text{O}_2 \rightarrow \text{O}_2^+ + \text{O}$	$k_2 = 2 \times 10^{-11} (\text{T}/300)^{-0.4}$
3	$\text{O}^+ + \text{NO} \rightarrow \text{NO}^+ + \text{O}$	$k_3 = 8 \times 10^{-13}$
4	$\text{O}^+ + \text{e} \rightarrow \text{O}(\text{P}) + h\nu_{1356}$	$k_4 = 7.3 \times 10^{-13}$
5	$\text{O}_2^+ + \text{N}_2 \rightarrow \text{NO}^+ + \text{NO}$	$k_5 = 5 \times 10^{-16}$
6	$\text{O}_2^+ + \text{NO} \rightarrow \text{NO}^+ + \text{O}_2$	$k_6 = 4.4 \times 10^{-10}$
7	$\text{O}_2^+ + \text{e} \rightarrow \text{O} + \text{O}$	$k_7 = 1.6 \times 10^{-7} (300/\text{T})^{0.55}$
8	$\text{N}_2^+ + \text{O} \rightarrow \text{NO}^+ + \text{N}$	$k_8 = 1.4 \times 10^{-10} (300/\text{T})^{0.44}$
9	$\text{N}_2^+ + \text{O} \rightarrow \text{O}^+ + \text{N}_2$	$k_9 = 1 \times 10^{-11} (300/\text{T})^{0.23}$
10	$\text{N}_2^+ + \text{O}_2 \rightarrow \text{O}_2^+ + \text{N}_2$	$k_{10} = 5 \times 10^{-11} (300/\text{T})^{-1}$
11	$\text{N}_2^+ + \text{NO} \rightarrow \text{NO}^+ + \text{N}_2$	$k_{11} = 3.3 \times 10^{-10}$
12	$\text{N}_2^+ + \text{e} \rightarrow \text{N} + \text{N}$	$k_{12} = 1.8 \times 10^{-7} (300/\text{T})^{0.39}$
13	$\text{NO}^+ + \text{e} \rightarrow \text{N} + \text{O}$	$k_{13} = 4.2 \times 10^{-7} (300/\text{T})^{0.85}$

**Table A2.** Chemical Production and Loss Rates

	Loss Rate, L (s <sup>-1</sup> )	Production (m <sup>-3</sup> s <sup>-1</sup> )
O <sup>+</sup>	k <sub>1</sub> N <sub>2</sub> + k <sub>2</sub> O <sub>2</sub> + k <sub>3</sub> NO + k <sub>4</sub> O	k <sub>9</sub> O N <sub>2</sub> <sup>+</sup>
O <sub>2</sub> <sup>+</sup>	k <sub>5</sub> N <sub>2</sub> + k <sub>6</sub> NO + k <sub>7</sub> e	k <sub>2</sub> O <sub>2</sub> O <sup>+</sup> + k <sub>10</sub> O <sub>2</sub> N <sub>2</sub> <sup>+</sup>
N <sub>2</sub> <sup>+</sup>	(k <sub>8</sub> + k <sub>9</sub> )O + k <sub>10</sub> O <sub>2</sub> + k <sub>11</sub> NO + k <sub>12</sub> e	
NO <sup>+</sup>	k <sub>13</sub> e	k <sub>1</sub> N <sub>2</sub> O <sup>+</sup> + k <sub>3</sub> NO O <sup>+</sup> + k <sub>5</sub> N <sub>2</sub> O <sub>2</sub> <sup>+</sup> + k <sub>6</sub> NO O <sub>2</sub> <sup>+</sup> + k <sub>8</sub> O N <sub>2</sub> <sup>+</sup> + k <sub>11</sub> NO N <sub>2</sub> <sup>+</sup>

low, and because the biggest response to the tsunami occurs in the F-region ionosphere.

## A2. Mean State Ion Densities

[44] We model the electron number density profile as a Chapman layer with the F2 peak at 300-km altitude with a maximum number density of 10<sup>12</sup> m<sup>-3</sup>, and with an E-layer peak at 105 km altitude and a number density of 1.25 × 10<sup>7</sup> m<sup>-3</sup>. Implicit in this choice of parameters is the assumption of nighttime conditions at moderately high solar activity. The Chapman layer is defined by

$$n_e(z) = N_{\max} \exp \left\{ 0.5 \left[ 1 - \frac{(z - z_{\max})}{H} - \exp \left( -\frac{(z - z_{\max})}{H} \right) \right] \right\} \quad (\text{A1})$$

where  $z_{\max}$  and  $N_{\max}$  are the height and value, respectively, of the maximum number density, and  $H$  is the atmospheric-scale height at either of the E-region or F-region peak. The total electron content (TEC) was calculated by integrating the electron density over altitude. Its undisturbed value was ∼17 TECU, where 1 TECU = 10<sup>16</sup> electrons m<sup>-2</sup>.

[45] We solve for the number densities of O<sup>+</sup>, N<sub>2</sub><sup>+</sup> and NO<sup>+</sup> by assuming charge neutrality to eliminate O<sub>2</sub><sup>+</sup>, and then solve the following matrix equation with chemical rate coefficients given by *Schunk and Sojka* [1996].

$$\begin{bmatrix} L(O^+) & -k_9O & 0 \\ k_1N_2 + k_3NO + k_{13}n_e & k_8O + k_{11}NO + k_{13}n_e & k_5N_2 + k_6NO + k_{13}n_e \\ -k_2O_2 & -k_{10}O_2 & L(O_2^+) \end{bmatrix} \begin{bmatrix} O^+ \\ N_2^+ \\ NO^+ \end{bmatrix} = \begin{bmatrix} 0 \\ k_{13}n_e^2 \\ 0 \end{bmatrix} \quad (\text{A2})$$

## A3. Ion Dynamics

[46] We use the approach of *McLeod* [1965] and neglect polarization electric fields and diffusion.

$$\vec{v}_i = (\omega_i^2 + \nu_{in}^2)^{-1} \left\{ \nu_{in} \omega_i \vec{U} \times \hat{B} + \omega_i^2 (\vec{U} \cdot \hat{B}) \hat{B} + \nu_{in}^2 \vec{U} \right\} \quad (\text{A3})$$

where  $\vec{U}$  is the neutral gas velocity,  $\omega_i = q_i B / M_i$  is the ion gyrofrequency and  $\nu_{in} = 2.6 \times 10^{-15} (n_n + n_i) A^{-1/2}$  [Kelley, 1989] is the ion-neutral collision frequency, and where  $q_i$  and  $M_i$  are the charge and atomic or molecular weight, respectively of the ion,  $B$  is the magnetic field strength in Gauss (Wb/m<sup>2</sup>),  $n_n$  and  $n_i$  are the neutral and ion number density, respectively, and  $A$  is the mean neutral molecular mass (in amu). All units are mks. Note that the ion gyrofrequency is species dependent and approximately altitude independent while the ion-neutral collision frequency is altitude dependent but not species dependent.

[47] The magnetic field vector is defined in terms of the magnetic dip angle,  $I$ .

$$\hat{B}/B = \hat{i} \cos I + \hat{k} \sin I. \quad (\text{A4})$$

A simple dipole field is assumed and the dip angle  $I$  is related to latitude  $\theta$  by the following.

$$\sin I = -2 \sin \theta / \sqrt{1 + 3 \sin^2 \theta}$$

and

$$\cos I = -\cos \theta / \sqrt{1 + 3 \sin^2 \theta}$$

where  $\hat{i}$  and  $\hat{k}$  are positive due south and upward, respectively (the same convention used in the full-wave model). Hence  $\hat{B}$  is directed northward and downward in the northern hemisphere.

[48] Defining the neutral velocity as  $\vec{U} = u\hat{i} + v\hat{j} + w\hat{k}$  then (A3) becomes

$$\begin{aligned} (\omega_i^2 + \nu_{in}^2) \vec{v}_i = & \{ \nu_{in} \omega_i v \sin I + \omega_i^2 (u \cos I + w \sin I) \cos I + \nu_{in}^2 u \} \hat{i} \\ & + \{ \nu_{in} \omega_i (w \cos I - u \sin I) + \nu_{in}^2 v \} \hat{j} \\ & + \{ -\nu_{in} \omega_i v \cos I + \omega_i^2 (u \cos I + w \sin I) \sin I + \nu_{in}^2 w \} \hat{k} \end{aligned} \quad (\text{A5})$$

The neutral perturbation velocity components in equation (A5) are obtained directly from the full-wave model. The velocity divergence was calculated by assuming plane waves in the horizontal direction with wavenumbers  $k$  and  $l$ , and by finite differencing the vertical component of the ion velocity:  $\nabla \cdot \vec{v}_i = -iku_i - ilv_i + \partial w_i / \partial z$ .

## A4. Perturbation Ion Densities

[49] For each ion species  $n_j$  we solve the continuity equation

$$\frac{\partial n_j'}{\partial t} + w_j' \frac{d\bar{n}_j}{dz} + \bar{n}_j \nabla \cdot \vec{v}_j' = P_j' - (n_j L_j)'. \quad (\text{A6})$$

or

$$i\omega n_j' + w_j' \frac{d\bar{n}_j}{dz} + \bar{n}_j \nabla \cdot \vec{v}_j' = P_j' - \bar{n}_j L_j' - n_j' \bar{L}_j \quad (\text{A7})$$

The ion velocities in equation (A7) are obtained from equation (A5). Mean ion-scale heights were calculated using finite differences from the solutions of equation (A2). Linearization of the chemical terms appearing in equation (A7) is similar to previous airglow perturbation work [Walterscheid et al., 1987; Hickey, 1988]. Temperature-dependent rate constants

of the form  $k = \bar{k}T^{-b}$  create terms of the form  $k' = T' \partial k / \partial T = -b \bar{k} T' / \bar{T}$ . We assume that perturbations of  $O_2$ ,  $N_2$  and  $O$  are all described by the full-wave model, which means we assume they constitute the major gas. Hence for any of these species we can write

$$\frac{n'(O)}{\bar{n}(O)} = \frac{n'(O_2)}{\bar{n}(O_2)} = \frac{n'(N_2)}{\bar{n}(N_2)} = \frac{M'}{M} \quad (A8)$$

Equation (A7) is written concisely in matrix form as  $An'_i = B$ , where  $n'_i = [O^+ \ N_2^+ \ NO^+ \ O_2^+]^T$ .

[50] **Acknowledgments.** M.P.H. was supported by the National Science Foundation under grants ATM-0408407 and ATM-0639293. G.S. acknowledges support from the NASA Mars Fundamental Research program under grant NNG05GM06G. R.L.W. was supported by NASA grant NNX08AM13G and by NSF grant ATM 0737557.

[51] Amitava Bhattacharjee thanks Philippe Lognonne and another reviewer for their assistance in evaluating this paper.

## References

- Abe, K. (2006), Dominant periods of the 2004 Sumatra tsunami and the estimated source size, *Earth Planets Space*, **58**, 217–221.
- Artru, J., V. Ducic, H. Kanamori, P. Lognonne, and M. Murakami (2005a), Ionospheric detection of gravity waves induced by tsunamis, *Geophys. J. Int.*, **160**, 840–848.
- Artru, J., P. Lognonne, G. Occhipinti, F. Crespon, R. Garcia, E. Jeansou, and M. Murakami (2005b), Tsunami detection in the ionosphere, *Space Res. Today*, **163**, 23–27.
- Bruce, G. H., D. W. Peaceman, H. H. Rachford Jr., and J. D. Rice (1953), Calculations of unsteady-state gas flow through porous media, *Trans. AIME*, **198**, 79–92.
- Georges, T. M. (1968), HF Doppler studies of traveling ionospheric disturbances, *J. Atmos. Terr. Phys.*, **30**, 735–746.
- Hedin, A. E. (1991), Extension of the MSIS thermosphere model into the middle and lower atmosphere, *J. Geophys. Res.*, **96**, 1159–1172.
- Hedin, A. E., et al. (1996), Empirical wind model for the upper, middle and lower atmosphere, *J. Atmos. Terr. Phys.*, **58**, 1421–1447.
- Hickey, M. P. (1988), Effects of eddy viscosity and thermal conduction and Coriolis force in the dynamics of gravity wave-driven fluctuations in the OH nightglow, *J. Geophys. Res.*, **93**, 4077–4088.
- Hickey, M. P., R. L. Walterscheid, M. J. Taylor, W. Ward, G. Schubert, Q. Zhou, F. Garcia, M. C. Kelley, and G. G. Shepherd (1997), Numerical simulations of gravity waves imaged over Arecibo during the 10-day January 1993 campaign, *J. Geophys. Res.*, **102**, 11,475–11,489.
- Hickey, M. P., R. L. Walterscheid, and P. G. Richards (2000), Secular variations of atomic oxygen in the mesopause region induced by transient gravity wave packets, *Geophys. Res. Lett.*, **27**, 3599–3602.
- Hickey, M. P., G. Schubert, and R. L. Walterscheid (2001), Acoustic wave heating of the thermosphere, *J. Geophys. Res.*, **106**, 21,543–21,548.
- Hines, C. O. (1972), Gravity waves in the atmosphere, *Nature*, **239**, 73–78.
- Huang, T.-Y., and M. P. Hickey (2008), Secular variations of OH nightglow emission and of the OH intensity-weighted induced by gravity wave forcing in the MLT region: On the distribution and transport of minor species, *Adv. Space Res.*, **41**, 1477–1486, doi:10.1016/j.asr.2007.10.020.
- Kelley, M. C. (1989), *The Earth's Ionosphere*, Academic, San Diego, Calif.
- Kubota, M., H. Fukunishi, and S. Okano (2001), Characteristics of medium- and large-scale TIDs over Japan derived from OI 630-nm nightglow observation, *Earth Planets Space*, **53**, 741–751.
- Lee, M. C., R. Pradipta, W. J. Burke, A. Labno, L. M. Burton, J. A. Cohen, S. E. Dorfman, A. J. Coster, M. P. Sulzer, and S. P. Kuo (2008), Did tsunami-launched gravity waves trigger ionospheric turbulence over Arecibo?, *J. Geophys. Res.*, **113**, A01302, doi:10.1029/2007JA012615.
- Lighthill, J. (1978), *Waves in Fluids*, Cambridge Univ. Press, Cambridge, U. K.
- Lindzen, R. S., and H. L. Kuo (1969), A reliable method for the numerical integration of a large class of ordinary and partial differential equations, *Mon. Weather Rev.*, **97**, 732–734.
- Liu, J. Y., Y. B. Tsai, S. W. Chen, C. P. Lee, Y. C. Chen, H. Y. Yen, W. Y. Chang, and C. Lui (2006), Giant ionospheric disturbances excited by the M9.3 Sumatra earthquake of 26 December 2004, *Geophys. Res. Lett.*, **33**, L02103, doi:10.1029/2005GL023963.
- Marsh, D., S. C. Solomon, and A. E. Reynolds (2004), Empirical model of nitric oxide in the lower thermosphere, *J. Geophys. Res.*, **109**, A07301, doi:10.1029/2003JA010199.
- Martinis, C., J. Baumgardner, S. M. Smith, M. Colerico, and M. Mendillo (2006), Imaging science at El Leoncito, Argentina, *Ann. Geophys.*, **24**, 1375–1385.
- McLeod, M. A. (1965), Sporadic E theory. I. Collision-geomagnetic equilibrium, *J. Atmos. Sci.*, **23**, 96–109.
- Mendillo, M., J. Baumgardner, D. Nottingham, J. Aarons, B. Reinisch, J. Scali, and M. C. Kelley (1997), Investigations of thermospheric-ionospheric dynamics with 6300-Å images from the Arecibo Observatory, *J. Geophys. Res.*, **102**, 7331–7343.
- Occhipinti, G., P. Lognonne, E. A. Kherani, and H. Hebert (2006), Three-dimensional waveform modeling of ionospheric signature induced by the 2004 Sumatra tsunami, *Geophys. Res. Lett.*, **33**, L20104, doi:10.1029/2006GL026865.
- Occhipinti, G. E., A. Kherani, and P. Lognonne (2008), Geomagnetic dependence of ionospheric disturbances induced by tsunamigenic internal gravity waves, *Geophys. J. Int.*, **173**, 753–765.
- Orlanski, I., and K. Bryan (1969), Formation of the thermocline step structure by large-amplitude internal gravity waves, *J. Geophys. Res.*, **74**, 6975–6983.
- Peltier, W. R., and C. O. Hines (1976), On the possible detection of tsunamis by a monitoring of the ionosphere, *J. Geophys. Res.*, **81**, 1995–2000.
- Rabinovich, A. B., and R. E. Thomson (2007), The 26 December 2004 Sumatra tsunami: Analysis of tide gauge data from the world ocean. Part 1: Indian Ocean and South Africa, *Pure Appl. Geophys.*, **164**, 261–308, doi:10.1007/s00024-006-0164-5.
- Rees, M. H. (1989), *Physics and Chemistry of the Upper Atmosphere*, Cambridge Univ. Press, New York.
- Schubert, G., M. P. Hickey, and R. L. Walterscheid (2005), Physical processes in acoustic wave heating of the thermosphere, *J. Geophys. Res.*, **110**, D07106, doi:10.1029/2004JD005488.
- Schunk, R., and J. Sojka (1996), USU model of the global ionosphere, in *STEP: Handbook of Ionospheric Models*, edited by R. W. Schunk, SCOSTEP, Logan, Utah.
- Taylor, M. J., J.-M. Jahn, S. Fukao, and A. Saito (1998), Possible evidence of gravity wave coupling into the mid-latitude F region ionosphere during the SEEK campaign, *Geophys. Res. Lett.*, **25**, 1801–1804.
- Walterscheid, R. L., and M. P. Hickey (2001), One-gas models with height-dependent mean molecular weight: Effects on gravity wave propagation, *J. Geophys. Res.*, **106**, 28,831–28,839.
- Walterscheid, R. L., G. Schubert, and J. Straus (1987), A dynamical-chemical model of wave-driven fluctuations in the OH nightglow, *J. Geophys. Res.*, **92**, 1241–1254.

M. P. Hickey, Department of Physical Sciences, Embry-Riddle Aeronautical University, 600 S. Clyde Morris Boulevard, Daytona Beach, FL 32114, USA. (hickey0b5@erau.edu)

G. Schubert, Department of Earth and Space Sciences and Institute of Geophysics and Planetary Physics, University of California, 595 Circle Drive East, Los Angeles, CA 90095-1567, USA.

R. L. Walterscheid, Space Science Applications Laboratory, The Aerospace Corporation, M2-260, 2350 East El Segundo Boulevard, El Segundo, CA 90245-4691, USA.